

# An Approach to Condition Monitoring of BLDC Motors with Experimentally Validated Simulation Data

Max Weigert<sup>1</sup>

<sup>1</sup>*Institute of Flight Systems and Automatic Control, Technical University of Darmstadt, Otto-Berndt-Str. 2, 64287 Darmstadt, Germany*

*weigert@fsr.tu-darmstadt.de*

## ABSTRACT

Due to their compact design and low number of wear parts, Brushless Direct Current (BLDC) motors are ideally suited for use in unmanned aerial vehicles (UAVs). In view of the growing areas of application and the increasing complexity of unmanned flight missions, the need for suitable safety mechanisms for the operation of technical components, such as BLDC motors, in unmanned aircraft drive trains is also increasing. The integration of redundant components analogous to manned aviation is often not possible for smaller unmanned aerial vehicles for weight reasons. Therefore, online-capable dynamic diagnosis and prognosis methods for monitoring safety-critical components of unmanned aircraft are subject of ongoing research.

One major challenge in the development of data based condition monitoring approaches for safety critical components is the availability of operational data of degraded components. This often leads to an unbalanced database without sufficient information on components' degradation behavior.

In the presented work, this problem is approached by combining bench testing and simulation models. On a test rig, common degradation effects are recreated by targeted manipulation. This allows for a safe and expressive data acquisition of the components' behavior. In order to reduce the material and time required to build up a sufficient database for condition monitoring with experimental data, the observable effects are replicated in a simulation. This provides the opportunity to create a large database with slight variations in simulation parameters and incorporated noise in the simulation.

The BLDC motor manipulation on the test rig includes mechanical, electrical and magnetic manipulation. The effects of the manipulation are analyzed and their representation by parameters in the corresponding simulation

is derived. The model is built in MATLAB Simulink and replicates both the electrical and physical behavior of the motor, as well as its commutation behavior.

The established simulation data shall be used as a balanced dataset on which condition monitoring algorithms can be trained. This will allow for the comparison of various data based condition monitoring methods in the future. A remaining challenge lies in the time behavior of the analyzed degradation, which has not yet been explored in depth. The proposed approach might also be applied to further unmanned aerial vehicle components, such as servo motors.

## 1. INTRODUCTION

A meaningful assessment of the flight risk of UAVs is an important basis towards their increased use and enhanced automatization. The influence of different UAV components on its safety has therefore already been thoroughly discussed in the literature. Shafiee, Zhou, Mei, Dinmohammadi, Karama and Flynn (2021) conducted a fault tree and a failure mode and effects analysis (FMEA) for UAV failures during inspection of offshore wind turbines. In their FMEA, the risk of motor bearing failures was assigned the second highest priority after the risk of lack of battery power, which is not directly connected to the components' health. A similar FMEA was performed by Wang, Ng, Elhadidi, Ang and Moon (2019), who also studied the structure of the UAV with a finite element simulation. They as well assigned the second highest risk to the motor and electronic speed controllers (ESCs) after the battery. Osborne, Lantair, Shafiq, Zhao, Robu, Flynn and Perry (2019) conducted a survey with commercial UAV operators and summarized their assessment of UAV component safety. Their participants rated BLDC motor failures as relatively unlikely but attributed better warning of electrical and mechanical failures as the second highest priority for increasing UAV safety.

Analyzing possible failure mechanisms of BLDC motors is mostly done on corresponding test rigs. At the Institute for Flight Systems and Automatic control, this has already been done by Haus, Mikat, Nowara, Kandukuri, Klingauf, and

Max Weigert. This is an open-access article distributed under the terms of the Creative Commons Attribution 3.0 United States License, which permits unrestricted use, distribution, and reproduction in any medium, provided the original author and source are credited.

Buderath (2013) and by Wolfram, Vogel, and Stauder (2018). Haus et al. (2013) conducted a motor current signature analysis for asynchronous motors. They induced motor abnormalities by grinding the inner ring of the bearing with an angle grinder, short-circuiting stator windings together, and creating imbalances in the rotor. Wolfram et al. (2018) built up the test rig used in this work. They aimed for condition monitoring of multicopter drive trains by examining the input and output power of their components. Faults were generated by notches on the propeller and applying diamond paste into the bearing.

An overview of faults in BLDC motors is given by Kudelina, Asad, Vaimann, Rassolkin, Kallaste and Lukichev (2020). They differentiate mechanical failures, most often associated with the bearing, electrical failures and permanent magnet failures. Experimental replication of such failures has also been approached by Shifat and Hur (2020). They introduced short circuits of the BLDC coils, both in the same and in neighboring phases. Yang, Habibullah, Zhang, Xu, Lim and Nadarajan (2016) studied accelerated thermal aging of electrical motors. Repeated heating cycles of motors in an oven could clearly be associated with a health indicator based on their constructed features. Siddiolo and Buderath (2018) developed a prognostic framework for the Remaining Useful Lifetime (RUL) of aeronautic fan ball bearings. For their Run-to-Failure tests, they introduced diamond-powder into the bearing.

The challenge of data-based condition monitoring based on experimental motor studies is the small database generated. To overcome this problem, this work aims at building up a simulation model of a BLDC motor and recreating degradation mechanisms in the simulation. This approach is for example also proposed in (Wolfram et al. 2018) and (Siddiolo and Buderath 2018).

The Simulation of BLDC motor behavior is based on its mathematical description. The underlying physical principles are for example discussed in (Hanselman 1994). A detailed derivation of the voltage profile for pulse width modulation commutation is given in (Baldursson 2005). Zhang, Liu, Peng and Liu (2020) used a mathematical model of a BLDC motor, to compare its healthy state with one involving an increased inverter resistance in one phase. Gupta, Jayaraman and Reddy (2021) as well simulated the BLDC motor behavior with increased resistance values and analyzed its effects on the motor behavior.

## 2. OPERATION OF THE BLDC MOTORS

This work exemplarily focuses on the components of the SciHunter UAV, which was built as a reference system at the institute. The UAV makes use of two different types of BLDC motors, four Multiplex ROXXY C42 motors are used for lift generation, one Multiplex ROXXY C35 motor is used for thrust generation. Both motor variations are designed as brushless outrunners with 14 magnetic poles on the rotor and

12 coils on the stator. They differ in their dimensions and performance according to their different operating requirements.

The thrust generating Multiplex ROXXY C35 is chosen as a starting point for the motor analysis. It is expected to be operated in the majority of the flight time, as the fixed wing flight with generated thrust is faster and more energy efficient compared to the hover flight. The behavior of the motor is analyzed for a constant thrust generation in uniform flight. This allows for a reduced complexity and good generalization of the data analysis. During flight, the motor is expected to be operated mainly in unaccelerated flight phases at the equilibrium. Therefore, those flight phases are providing both the largest amount of data for a data based condition monitoring and the most frequent opportunity to collect and analyze current flight data. The smaller variation in the sensor data due to the uniform operation of the motor in unaccelerated flight is an additional advantage that simplifies the interpretation of the created database. For a typical flight speed of 60 km/h picked out of the possible fixed wing flight speed range from 50 km/h to 72 km/h of the UAV, the motor has to provide 5.17 N of thrust based on the known drag coefficient of the UAV.

The picked operating point is approximated by having the motor rotate an airscrew generating the desired thrust both in the experimental setup and the created simulation model. The airspeed during flight is neglected for the initial data collection, as it is not expected to significantly affect the effects of degradation on the motor. Both the test rig and the simulation provide the opportunity to integrate operating conditions of higher complexity in the future by airspeed or varying motor speed.

### 2.1. Experimental Setup

The experimental setup utilizes the existing test rig of the institute. The test rig is visualized in Figure 1. The motor is operated by the Electronic Speed Controller (ESC) FrSky Neuron 60, which is also deployed in the SciHunter. The ESC can be controlled from LabView, where the test procedure is coordinated and the measured data is collected. It is connected to a switched-mode power supply with a DC voltage of 14.8 V, equivalent to the battery voltage of the UAV. For the uniform operation profile, the motor is equipped with its corresponding airscrew and a duty cycle of 48 % is set for the ESC, which results in a rotational motor speed of approximately 3660 rotations per minute (rpm) and the desired thrust of 5.17 N generated by the airscrew.

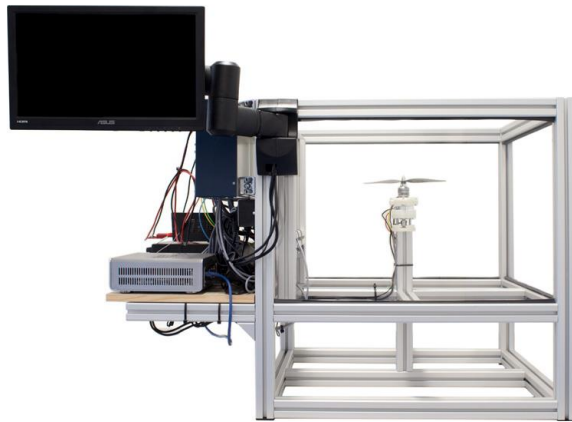


Figure 1. Test rig setup by (Wolfram et al. 2018).

The motor is mounted on top of a force and a torque sensor and a thermocouple is inserted in the stator next to its windings. The rotational speed of the motor is measured by an optical infrared measurement. A measuring board equipped with current and voltage sensors is used to observe the supply current of the ESC and the phase currents from the ESC to the motor. In future measurement series, the telemetry data of the ESC might also be collected and used as a reference for voltage, current and speed measurements.

### 2.2. Mathematical Modelling

To describe the motor behavior with physical equations, the abstracted circuit diagram in Figure 2 is utilized. It represents the ESC switches used for commutation and the coils of the three different phases, which are connected in a star configuration. Each depicted coil represents 4 stator coils, which are connected in series in the described motor. Compared to the simplest possible coil configuration with one coil per phase and two magnet poles, its back electromotive force (EMF) with 14 magnetic poles is periodic for one seventh of the motor rotation and it is assumed to be ideally trapezoidal shaped. Interactions between the coils are neglected in the presented modelling.

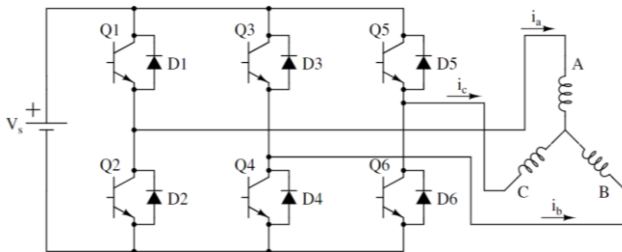


Figure 2. BLDC drive scheme (Baldursson 2005).

The switching behavior of the ESC is based on the current position of the motor. For every seventh of a motor rotation,

6 commutation configurations are gone through. Each of them features one coil with positive, one with negative and one with no applied voltage. The 6 configurations can be summarized by the two variations of the circuit diagram shown in Figure 3, which can both be applied for the three current combinations  $i_a$  &  $i_b$ ,  $i_b$  &  $i_c$  and  $i_c$  &  $i_a$  as  $i_1$  &  $i_2$ . Additionally shown in Figure 4 are the two variations of the circuit diagram derived with only one closed switch for each current combination. Those configurations are assumed to be present when the pulse width modulation signal is 0 and the voltage supply shall be temporarily withdrawn. The ratio of active and inactive pulse width modulation signal is specified by the duty cycle. The switches and diodes of the ESC are assumed as ideal and their physical behavior is not accounted for. This allows for the derivation of the voltage difference between each of the phases, depending on the motor position. For a detailed statement of all derivable voltage equations, refer to (Baldursson 2005).

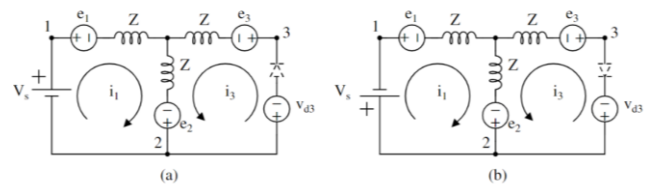


Figure 3. Commutation variations with voltage supply (Baldursson 2005).

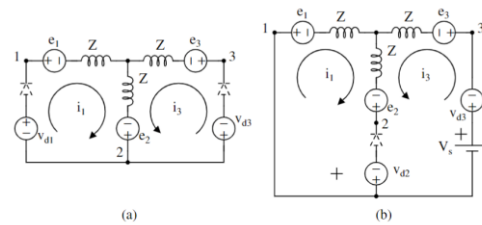


Figure 4. Commutation variants without voltage supply (Baldursson 2005).

The currents in the three phases can then be derived based on the mesh equations between the phases a & b and b & c. In accordance with the star connection, the current of the third phase can be calculated as the negative sum of the other two phases. Therefore, only two currents are calculated with differential equations and only two voltage differences supply sufficient information. Those current derivatives are given in Eq. 1 and Eq. 2 with the voltage differences  $v_{eab}$  and  $v_{ebc}$  already denoting the voltage less the back EMF differences from the respective phases.

$$\begin{aligned} & \frac{d}{dt} * i_a \\ & = ((L_b + L_c) * ve_{ab} + L_b * ve_{bc} \\ & - (L_b * R_a + L_b * R_c + L_c * R_a) \cdot i_a \\ & + (-L_b * R_c + L_c * R_b) * i_b) \\ & * \frac{1}{L_a \cdot L_b + L_a \cdot L_c + L_b \cdot L_c} \end{aligned} \quad \text{Eq. 1}$$

$$\begin{aligned} & \frac{d}{dt} * i_b \\ & = (-L_c * ve_{ab} + L_a * ve_{bc} \\ & + (-L_a * R_c + L_c * R_a) * i_a \\ & - (L_a * R_b + L_a * R_c + L_c * R_b) * i_b) \\ & * \frac{1}{L_a * L_b + L_a * L_c + L_b * L_c} \end{aligned} \quad \text{Eq. 2}$$

The electric moment is calculated based on the obtained phase currents according to Eq. 3. It is in equilibrium with the product of inertia and acceleration, the airscrew torque and the frictional torque.

$$\begin{aligned} T_e & = \frac{e_a * i_a + e_b * i_b + e_c * i_c}{\dot{\Theta}_m} \\ & = \frac{k_e}{2} * (f_a * i_a + f_b * i_b + f_c * i_c) \end{aligned} \quad \text{Eq. 3}$$

The generator constant  $k_e$  and the resistance are both approximated as linearly temperature dependent, the generator constant with a negative and the resistance with a positive proportionality factor. The motor temperature difference to the ambient temperature is described in a simplified way by the product of the power loss and the thermal resistance between windings, housing and environment. In the simulation, the time behavior of the motor heating is modeled with a  $PT_1$  transmission behavior. To avoid simulating long warm-up processes, a smaller time constant for the motor startup can be enabled.

### 3. REPLICATION OF DEGRADATION EFFECTS

To build up an expressive database for the development of data based condition monitoring and prognosis methods, this work aims at replicating degradation effects on the considered component. For this purpose, the regarded motor was manipulated on a test rig and a simulation model of the engine accounting for different degradation effects was built up.

#### 3.1. Test rig

On the test rig, mechanical, electrical and magnetic manipulation of the motor was pursued. To achieve distinctive, traceable, and timely results, active adjustments were made to the motor. Long-term run to failure tests without active advancement of specific degradation

mechanisms might be supplementarily carried out in the future.

#### 3.1.1. Mechanical Manipulation of the Motor

The motor bearings were identified as primary source of mechanical failure. To intensify the bearing degradation by increased friction and abrasion, diamond powder was inserted in the bearing. A run to failure test with the manipulated motor was carried out. The measurement was characterized in particular by a sudden failure of the motor. Cause of the fault was a broken rolling element cage, as depicted in Figure 5. The measurement was conducted with a periodical measurement interval, as a constant degradation trend was expected. Unfortunately, the failure occurred in between two measurement periods. For further analysis, a more sophisticated measurement method is planned, in which measurement data shall first be stored temporarily and then be largely deleted again if there are no significant changes in the system behavior.



Figure 5. Motor with broken bearing cage.

#### 3.1.2. Electrical Manipulation of the Motor

To manipulate the electrical behavior of the motor, two methods have been utilized. A winding short circuit was introduced by a solder drop on a motor coil and the phase resistance was increased by connecting a series resistor.

With the solder drop, covering approximately 20 % of one coil, neighboring windings on multiple winding levels have been short circuited. An image of the manipulated stator is given in Figure 6. In particular, the behavior in the event of local damage to the insulation and increased heat build-up should be simulated, which might particularly affect neighboring windings on several winding levels. The effects of the solder drop are clearly visible on the test bench and the achievable motor speed at the specified duty cycle of 48 % drops from 3660 rpm to 3315 rpm.



Figure 6. Manipulated stator with solder drop.

By introducing various series resistors, degradation effects due to coil material aging or temperature raises with declining efficiency shall be addressed. The effects of the series resistors are clearly visible, leading to an increasing drop in motor speed with increasing series resistance for a fixed duty cycle. The series resistor was connected with one phase of the motor, which lead to a decreased current in that phase, while the currents in the remaining phases slightly increased with decreasing motor speed.

### 3.1.3. Magnetic Manipulation of the Motor

The magnetic field of the rotor was manipulated by heating the rotor at 220 °C for one hour. The magnetic flux density of the rotor was measured before and after the heating process with a 3-axis magnetic field sensor and approximately halved in size. The effects of the reduced magnetic field resulting in higher currents and a higher resulting motor speed at the same duty cycle are also clearly visible.

## 3.2. Simulation

A Simulation Model of the motor has been built up in MATLAB Simulink. It relies on the mathematical description of the motor introduced in chapter 2.2. Beside its replication of the nominal motor behavior, 10 kinds of degradation mechanisms can be recreated in the model. Up to now, these mechanisms have only been individually activated for simulations, but they can also be enabled in combination with each other for an even broader database.

To ensure a high amount of unique simulation outputs, the coil inductivities and resistances can be slightly varied for each simulation. Additionally, the ambient temperature can have noise applied to it. This affects the airscrew torque as well as the resistances and generator constant. Therefore, it replicates the dependency of the motor of its environment, which might introduce variations in its behavior on the test rig.

### 3.2.1. Mechanical Degradation Recreation

To model mechanical degradation in the simulation, four degradation aspects are considered. Those involve increased bearing friction, periodic bearing loads, static eccentricity effects and dynamic eccentricity.

The increasing bearing friction with time can directly be implemented. It depicts the results of contamination in the bearing, loss or exhaustion of the lubricant and deteriorated rolling characteristics due to abrasion. In reference to bearing lifetime estimations by bearing manufacturers, a growth of the friction coefficient is implemented as a function of normalized torque, normalized rotational speed and number of revolutions. With the aim of imitating a realistic bearing lifetime, changes in the defining degradation parameters as the bearing friction coefficient are nearly undetectable within the simulated timespans. For a condition monitoring, the simulation of distinguished degradation stages already offers valuable information, but the time behavior of the degradation effects remains of high interest for a holistic PHM system.

Periodic bearing loads resemble local deterioration effects like pitting. They are defined with a lookup table in Simulink and only present at a certain motor angle. The angle of the periodic bearing loads can be randomly varied for multiple simulations to achieve an extensive database.

Static eccentricity effects and dynamic eccentricity effects are expressed by a change in the trapezoidal functions of the back EMFs. For the dynamic eccentricity, the relative position of the stator axis to the rotor axis remains constant, and the back EMFs of the three phases are changed by static summands. They are derived as multiples of the sine of the eccentricity angle summed with the phase angles  $0$ ,  $2/3 \pi$  and  $4/3 \pi$ . For the static eccentricity, the relative position of the stator axis and the rotor axis change during the motor rotation. Therefore, the static eccentricity is calculated by adding the current rotation angle to the phase angles introduced for the dynamic eccentricity. A combination of both effects by adding summands representing both eccentricities at the same time is not yet implemented. Similar to the periodic bearing load, the angle of attack can be randomly varied to widen the simulated database.

### 3.2.2. Electrical Degradation Recreation

The degradation of the motor coils is represented by three short-circuit and two resistance increase variations. To broaden the simulation results, the coil numbers in the simulation can be switched. That way, it is ensured, that mechanisms affecting specific phases of the simulated motor can be acted out for all three phases.

The resistance increase in the simulation shall recreate the same effects as in the motor manipulation. In the simulation, increasing the resistance of a single coil specifically represents degradation effects due to local influences like

damaged insulation or polluted contacts, which might lead to higher temperatures and faster material aging. In another variation of the degradation mechanism, by increasing the resistance of all coils uniformly, degradation effects without designated points of attack are tackled.

Similar distinctions are made for the simulation of short circuits. Degradation effects without a specified point of attack are depicted as uniform winding failure. These are modeled under the simplifying assumption that all phases have internal short circuits in equal measure, as illustrated in Figure 7. Their short circuit ratio, expressing the number of short circuited windings divided by the overall winding number in each phase, is increased with the time of fault activity. This shall resemble a progressing failure of the insulations of adjacent windings due to increased heat development. The short circuits are assumed to be ideal, not presenting any resistance and reducing the effective resistance and inductivity with the factor  $(1-\mu)$ . The back EMF is assumed to be independent of the current flow in the short circuited windings. As only a part of the back EMF is passed by the current in each phase, the short circuit ratio is passed on as a factor to the created electric moment.

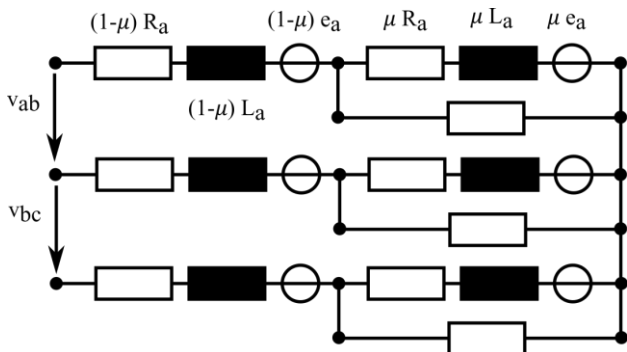


Figure 7. Circuit diagram with uniform short circuits.

For a single phase winding short circuit, the circuit diagram in Figure 8 is derived. The short circuit ratio is assumed to be at a fixed position, where the insulation might be compromised. With time, the resistance of the short circuit is expected to decrease towards zero. A new equation system describing the currents is derived from the circuit diagram, as given in Eq. 4 to Eq.6. It includes the short circuit current  $i_s$ . The electric moment is then calculated with respect to the effective currents passing the respective back EMF windings. For the short circuited phase, the product of the short circuit ratio and the short circuit current is subtracted from the phase current, as it resembles the share of back EMF, which is not passed by the short circuit current.

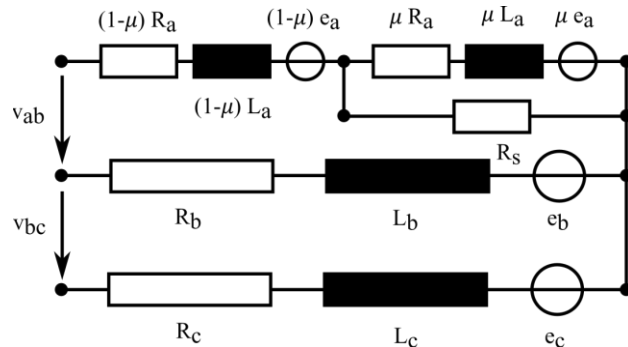


Figure 8. Circuit diagram with one phase short circuited.

$$\begin{aligned} \frac{d}{dt} * i_1 &= ((L_2 + L_3) * ve_{12} \\ &+ L_2 * ve_{23} \\ &+ (-L_2 + L_3) * R_1 * (1 - \mu) - L_2 * R_3) * i_1 \\ &+ (-L_2 * R_3 + L_3 * R_2) * i_2 \\ &+ (-L_2 + L_3) * R_s * i_s \\ &+ (L_2 + L_3) * e_1 * \mu \\ & * \frac{1}{L_1 * (1 - \mu) * (L_2 + L_3) + L_2 * L_3} \end{aligned} \quad \text{Eq. 4}$$

$$\begin{aligned} \frac{d}{dt} * i_2 &= (-L_3 * ve_{12} \\ &+ L_1 * (1 - \mu) * ve_{23} \\ &+ (-L_1 * (1 - \mu) * R_3 + L_3 * R_1 * (1 - \mu)) * i_1 \\ &+ - (L_1 * (1 - \mu) * (R_2 + R_3) + L_3 * R_2) * i_2 \\ &+ L_3 * R_s * i_s \\ &+ - L_3 * e_1 * \mu \\ & * \frac{1}{L_1 * (1 - \mu) * (L_2 + L_3) + L_2 * L_3} \end{aligned} \quad \text{Eq. 5}$$

$$\begin{aligned} \frac{d}{dt} * i_s &= ((L_2 + L_3) * ve_{12} \\ &+ L_2 * ve_{23} \\ &+ \left(-L_2 * R_3 + \frac{L_2}{L_1} * L_3 * R_1\right) * i_1 \\ &+ (-L_2 * R_3 + L_3 * R_2) * i_2 \\ &+ \left(-\left(L_2 + L_3\right) + \frac{L_2}{L_1} * L_3\right) * \left(\frac{R_s}{\mu} + R_1\right) \\ &+ (L_2 + L_3) * R_1 * \mu * i_s \\ &+ \left((L_2 + L_3) + \frac{L_2}{L_1} * L_3\right) * e_1 \\ & * \frac{1}{L_1 * (1 - \mu) * (L_2 + L_3) + L_2 * L_3} \end{aligned} \quad \text{Eq. 6}$$

A two phase winding short circuit is represented by the circuit diagram in Figure 9. Similar to the single phase short circuit, a new equation system can be derived, which accounts for the short circuit current as stated in Eq. 7 to Eq. 9. The short circuit ratios of the two phases are set as equal for the current simulations. The effective currents for the electric moment

calculation include the short circuit current in both affected phases factored with the respective short circuit ratio and opposing signs.

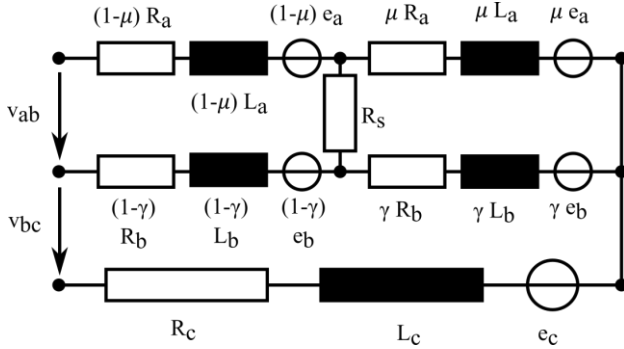


Figure 9. Circuit diagram with two phases short circuited.

$$\begin{aligned}
 & \frac{d}{dt} * i_a \\
 & = ((-L_2 * \gamma)^2 + (L_1 * \mu + L_2 * \gamma) * (L_2 \\
 & + L_3)) * v_{e12} \\
 & + L_2 * (1 - \gamma) * (L_1 * \mu + L_2 * \gamma) * v_{e23} \\
 & + (-L_2 * \gamma * ((R_1 + R_3) * L_2 * (1 - \gamma) + L_3 \\
 & * R_1 * (1 - \mu)) + L_1 * \mu * ((L_2 + L_3) * R_1 * (1 \\
 & - \mu) + L_2 * (1 - \gamma) * R_3)) * i_1 \\
 & + ((-R_3 * (L_1 * \mu + L_2 * \gamma) + L_3 * R_2 * (L_1 \\
 & * \mu / L_2 + \gamma)) * L_2 * (1 - \gamma)) * i_2 \\
 & + (-L_1 * \mu * R_s * (L_2 + L_3) + L_2 * \gamma \\
 & * (L_2 * (1 - \gamma) * R_1 * \mu - L_1 * \mu * R_2 * (1 - \gamma) \\
 & - L_3 * R_s)) * i_s \\
 & + (L_1 * \mu * (L_2 + L_3) + L_2 * \gamma * L_3) * (e_1 * \mu \\
 & - e_2 * \gamma) \\
 & / \left( L_1 * \mu * \left( \frac{(L_2 + L_3) * L_1 * (1 - \mu)}{+ L_3 * L_2 * (1 - \gamma)} \right) + L_2 * \gamma \right. \\
 & \left. * \left( \frac{(L_1 + L_3) * L_2 * (1 - \gamma)}{+ L_3 * L_1 * (1 - \mu)} \right) \right)
 \end{aligned}$$

Eq. 7

$$\begin{aligned}
 & \frac{d}{dt} * i_b \\
 & = ((-L_1 * \mu * L_2 * \gamma - (L_1 * \mu + L_2 * \gamma) * L_3) \\
 & * v_{e12} \\
 & + (L_1 * (1 - \mu) * (L_1 * \mu + L_2 * \gamma)) * v_{e23} \\
 & + ((L_1 * \mu + L_2 * \gamma) \\
 & * (L_3 * R_1 * (1 - \mu) - L_1 * (1 - \mu) * R_3)) * i_1 \\
 & + (-L_1 * (1 - \mu) * (L_1 * \mu * (R_2 + R_3) + L_2 \\
 & * R_3 * \gamma) - R_2 * (1 - \gamma) * ((L_1 + L_3) * L_2 * \gamma \\
 & + L_1 * L_3 * \mu)) * i_2 \\
 & + (L_1 * \mu * (-L_1 * (1 - \mu) * R_2 * \gamma + L_2 * \gamma \\
 & * R_1 * (1 - \mu)) + R_s * ((L_1 * \mu + L_2 * \gamma) * L_3 \\
 & + L_1 * L_2 * \gamma)) * i_s \\
 & + (-L_1 * L_2 * \gamma + (L_1 * \mu + L_2 * \gamma) * L_3) \\
 & * (e_1 * \mu - e_2 * \gamma) \\
 & / \left( L_1 * \mu * \left( \frac{(L_2 + L_3) * L_1 * (1 - \mu)}{+ L_3 * L_2 * (1 - \gamma)} \right) + L_2 * \gamma \right. \\
 & \left. * \left( \frac{(L_1 + L_3) * L_2 * (1 - \gamma)}{+ L_3 * L_1 * (1 - \mu)} \right) \right) \\
 & \frac{d}{dt} * i_s \\
 & = ((L_1 * L_2 * \mu + (L_1 * \mu + L_2 * \gamma) * L_3) \\
 & * v_{e12} \\
 & + (L_1 * \mu * L_2 - L_1 * L_2 * \gamma) * v_{e23} \\
 & + (L_2 * (\gamma - \mu) * (L_1 * R_3 - L_3 * R_1)) * i_1 \\
 & + (L_1 * (\mu - \gamma) * (L_3 * R_2 - L_2 * R_3)) * i_2 \\
 & + (-L_1 * (1 - \mu) * ((L_2 + L_3) * R_1 * \mu + L_3 \\
 & * R_2 * \gamma) + R_s * (L_1 * (L_2 + L_3) + L_2 * L_3) \\
 & + L_2 * (1 - \gamma) * ((L_1 + L_3) * R_2 * \gamma + L_3 * R_1 \\
 & * \mu)) * i_s \\
 & + (L_1 * (L_2 + L_3) + L_2 * L_3) * (e_1 * \mu - e_2 \\
 & * \gamma) \\
 & / \left( L_1 * \mu * \left( \frac{(L_2 + L_3) * L_1 * (1 - \mu)}{+ L_3 * L_2 * (1 - \gamma)} \right) + L_2 * \gamma \right. \\
 & \left. * \left( \frac{(L_1 + L_3) * L_2 * (1 - \gamma)}{+ L_3 * L_1 * (1 - \mu)} \right) \right)
 \end{aligned}$$

Eq. 8

Eq. 9

### 3.2.3. Magnetic Degradation Recreation

To represent a decrease in the magnetic flux density, which might be caused by too high motor temperatures or mechanical stresses, decreased trapezoidal functions of the back EMFs are applied in the simulation. This is assumed to be an adequate representation of magnetic degradation, as the back EMF can be described as a function of the coil dimensions, the magnetic flux density and the relative position of rotor and stator.

#### 4. OBSERVED BEHAVIOR

In order to investigate the validity of the simulation environment, the observed engine behavior on the test rig is compared with that from the simulation. Figure 10 and Figure 11 depict the phase currents on the test rig and in the simulation under healthy conditions. Both are shown under uniform operating conditions for a small time window, which allows distinguishing the commutation phases visible in the data. The model parameters have not yet been adjusted to match the test rig values, but the same behavior pattern is recognizable in both graphs. On the test rig, the commutation behavior of the ESC cannot be resolved in time though, while its resulting current fluctuations can be clearly seen in the simulation.

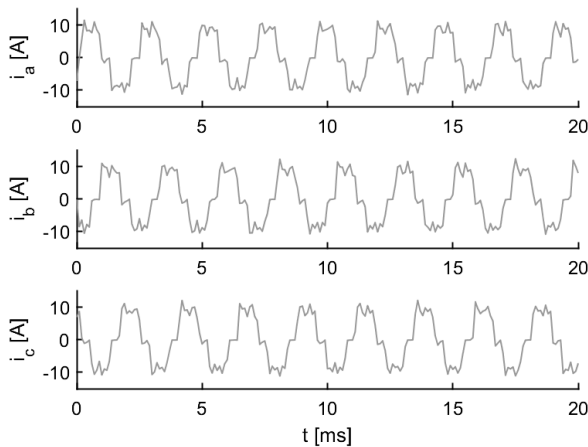


Figure 10. Test rig motor currents in healthy state.

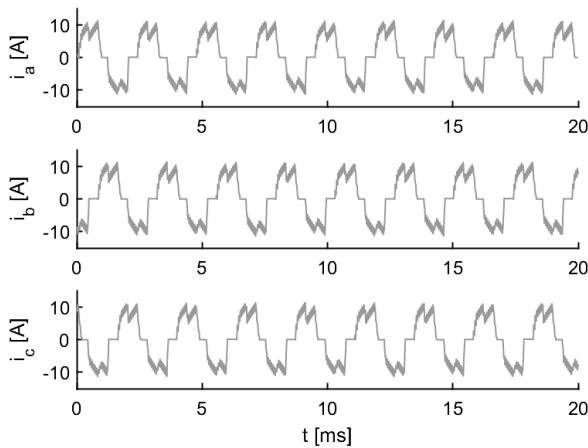


Figure 11. Simulation motor currents in healthy state.

With regard to the represented degradation mechanisms, the electrical failure mode of an increased resistance and the magnetic failure mode are shown as examples. As described in chapter 3.1.1, the behavior of the mechanical failure mode

could not be recorded completely and will therefore be investigated in future by means of further series of measurements. The failure mode behavior on the test rig and in the simulation are illustrated in Figure 12 to Figure 15 by the measured phase currents of a motor operated at the same duty cycle, as in the healthy state.

For both failure mechanisms, the observed behavior in experiment and simulation are well comparable. With the increased resistance in a single phase, a drop in the affected phase currents becomes visible. Simultaneously, a drop in the rotational speed occurs at a constant duty cycle. The decreased magnetic flux density leads to a slight increase in the rotational speed accompanied by an increase in the three phase currents.

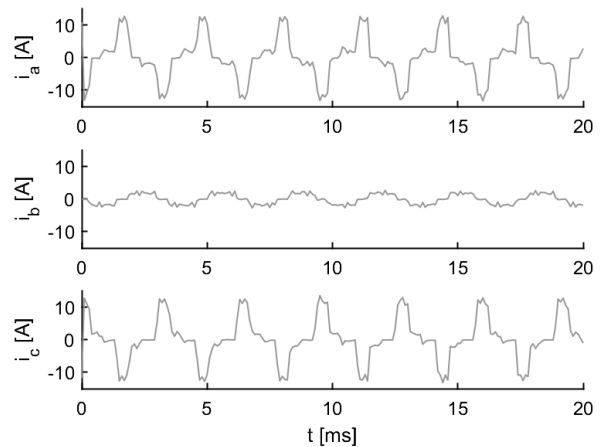


Figure 12. Test rig motor currents with increased resistance.

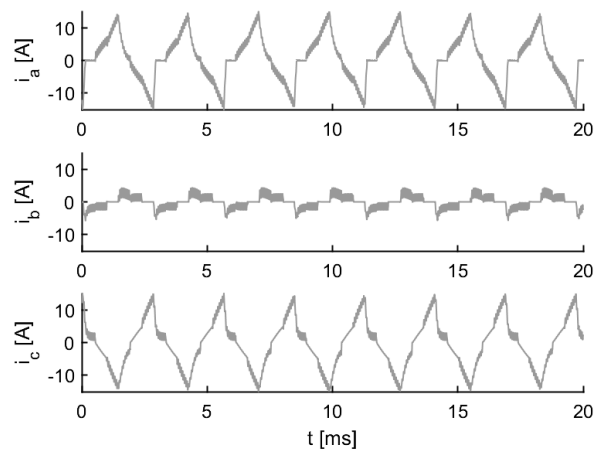


Figure 13. Simulation motor currents with increased resistance.

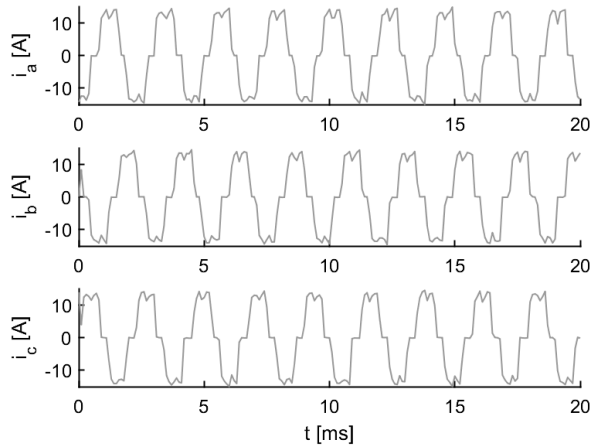


Figure 14. Test rig motor currents with demagnetization.

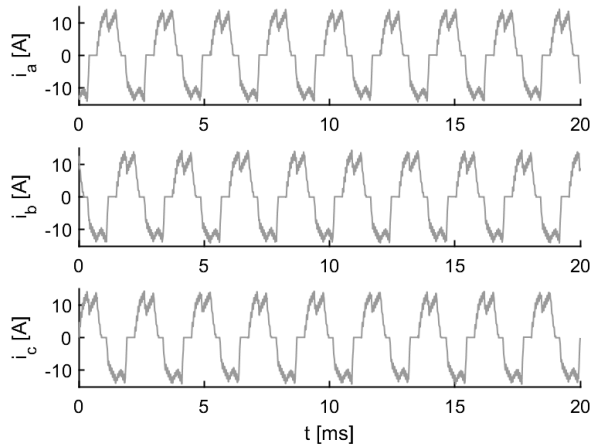


Figure 15. Simulation motor currents with demagnetization.

## 5. CONCLUSION AND OUTLOOK

In this paper, an approach is discussed to represent failure modes of BLDC motors experimentally and simulatively. This approach offers the potential to build up a large database for the application of data-based condition monitoring for BLDC engines. The presented work represents only an intermediate state. A more precise adaptation of the simulation parameters to reproduce the experimental results should increase their significance in the future. This starting point will then be used to derive meaningful features and to check the distinguishability of the considered fault cases by means of different machine learning methods.

The developed approach may then also enable a similar representation of the servo motor behavior, which are also safety-relevant components of the hybrid SciHunter UAV. The temporal relationship of the discussed degradation

mechanisms also requires further investigation. Longer-term Run-to-Failure tests may be conducted to investigate this in the future.

## ACKNOWLEDGEMENT

This project is funded by the Deutsche Forschungsgemeinschaft (DFG, German Research Foundation), whose support is highly appreciated by the author. Furthermore, the author would like to thank Mr. André Klütsch for his contributions to the test rig trials in the context of his master's thesis and Mr. Lorenz Dingeldein, for the exchange of simulation approaches for BLDC motors.

## NOMENCLATURE

$e$	back EMF
$f$	trapezoidal function
$k_e$	generator constant
$L$	inductivity
$R$	resistance
$t$	time
$T_e$	electric moment
$v$	voltage
$ve$	difference of voltage and back-EMF
$\mu$	first phase short circuit ratio
$\gamma$	second phase short circuit ratio
$\theta$	motor angle

## REFERENCES

- Baldursson, Stefán (2005): BLDC Motor Modelling and Control – A Matlab®/Simulink® Implementation. Chalmers University of Technology, Göteborg.
- Gupta, Annima; Jayaraman, Kalaiselvi; Reddy, Ravula Sugunakar (2021): Performance Analysis and Fault Modelling of High Resistance Contact in Brushless DC Motor Drive. In : IECON 2021 – 47th Annual Conference of the IEEE Industrial Electronics Society. IECON 2021 - 47th Annual Conference of the IEEE Industrial Electronics Society. Toronto, ON, Canada, 13.10.2021 - 16.10.2021: IEEE, pp. 1–6.
- Hanselman, Duane C. (Ed.) (1994): Brushless permanent-magnet motor design. New York: McGraw-Hill, Inc.
- Haus, Steffen; Mikat, Heiko; Nowara, Martin; Kandukuri, Surya; Klingauf, Uwe; Buderath, Matthias (2013): Fault Detection based on MCSA for a 400Hz Asynchronous Motor for Airborne Applications. In : International Journal of Prognostics and Health Management, vol. 4.
- Kudelina, Karolina; Asad, Bilal; Vaimann, Toomas; Rassolkin, Anton; Kallaste, Ants; Lukichev, Dmitri V. (2020): Main Faults and Diagnostic Possibilities of BLDC Motors. In : 2020 27th International Workshop on Electric Drives: MPEI Department of Electric Drives 90th Anniversary (IWED). 2020 27th International Workshop on Electric Drives: MPEI Department of